Article

Australian Bushfires (2019–2020): Aerosol Optical Properties and Radiative Forcing

Christina-Anna Papanikolaou [1,*] , **Panagiotis Kokkalis** [2] , **Ourania Soupiona** [1,3] , **Stavros Solomos** [4] , **Alexandros Papayannis** [1,5] , **Maria Mylonaki** [1] , **Dimitra Anagnou** [1] , **Romanos Foskinis** [1] **and Marilena Gidarakou** [1]

1   Laser Remote Sensing Unit, Department of Physics, National and Technical University of Athens, 15780 Zografou, Greece; raniaphd@mail.ntua.gr (O.S.); apdlidar@mail.ntua.gr (A.P.); mylonakimari@mail.ntua.gr (M.M.); dimiana@phys.uoa.gr (D.A.); foskinis@mail.ntua.gr (R.F.); ge16082@central.ntua.gr (M.G.)
2   Physics Department, Kuwait University, P.O. Box 5969, Safat 13060, Kuwait; panagiotis.kokkalis@ku.edu.kw
3   Raymetrics S.A., Spartis 32, 14452 Athens, Greece
4   Research Centre for Atmospheric Physics and Climatology, Academy of Athens, 10680 Athens, Greece; ssolomos@academyofathens.gr
5   LAPI, École Polytechnique Fédérale de Lausanne, 1015 Lausanne, Switzerland
*   Correspondence: papanikolaouca@mail.ntua.gr

Abstract: In the present study, we present the aerosol optical properties and radiative forcing (RF) of the tropospheric and stratospheric smoke layers, observed by the Cloud-Aerosol Lidar and Infrared Pathfinder Satellite Observation (CALIPSO) satellite, during the extraordinary Australian biomass burning (BB) event in 2019–2020. These BB layers were studied and analyzed within the longitude range 140° E–20° W and the latitude band 20°–60° S, as they were gradually transported from the Australian banks to the South American continent. These layers were found to be trapped within the Andes circulation, staying for longer time periods in the same longitude region. The BB aerosols reached altitudes even up to 22 km amsl., and regarding their optical properties, they were found to be nearly spherical (particle linear depolarization ratio (PLDR) < 0.10) in the troposphere; while, in the stratosphere, they were more depolarizing with PLDR values reaching up to 0.20. Fine and ultrafine smoke particles were dominant in the stratosphere, according to the observed Ångström exponent, related to the backscatter coefficients obtained by the pair of wavelengths 532 and 1064 nm (Å_b up to 3), in contrast to the Å_b values in the troposphere ($\text{Å}_b < 1$) indicative of the presence of coarser particles. As the aerosols fend off the source, towards North America, a slightly descending trend was observed in the tropospheric Å_b values, while the stratospheric ones were lightly increased. A maximum aerosol optical depth (AOD) value of 0.54 was recorded in the lower troposphere over the fire spots, while, in the stratosphere, AOD values up to 0.29 were observed. Sharp changes of carbon monoxide (CO) and ozone (O_3) concentrations were also recorded by the Copernicus Atmosphere Monitoring Service (CAMS) in various atmospheric heights over the study region, associated with fire smoke emissions. The tropospheric smoke layers were found to have a negative mean radiative effect, ranging from -12.83 W/m^2 at the top of the atmosphere (TOA), to -32.22 W/m^2 on the surface (SRF), while the radiative effect of the stratospheric smoke was estimated between -7.36 at the TOA to -18.51 W/m^2 at the SRF.

Keywords: Australian bushfires; biomass burning aerosols; tropospheric aerosols; stratospheric aerosols; CALIPSO; optical properties; ozone; carbon monoxide; radiative forcing

1. Introduction

Smoke aerosols affect the Earth's climate system in both direct and indirect ways, as they can highly absorb the sunlight due to their high content of black carbon (BC), but they can also modify the cloud properties (i.e., cloud life-time, precipitation, and ice formation) [1–6]. Freshly emitted soot particles are initially hydrophobic, but become hydrophilic

as a result of aging. Additionally, they can undergo compaction upon humidification, thus increasing their ability to serve as Cloud Condensation Nuclei (CCN) [7].

The impact of smoke particles on the climate also depends on their horizontal and vertical distributions, as well as on their chemical composition [8,9]. During long-range transport, there is evidence that the optical properties of smoke particles change [7,10], and different optical properties are commonly associated with the altitude range of the plumes [11,12]. Stratospheric smoke aerosols have significantly longer lifetimes than tropospheric ones, which increases the impact on Earth's atmosphere radiation budget. In general, smoke particles are one of the key aerosol types in climate research, thus the study of their vertical stratification, both in the troposphere and stratosphere, along with their optical and radiative properties, has become an urgent need, especially regarding extreme biomass burning (BB) events.

Apart from a major source of particulate matter (PM), BB is also an important source of trace gases in the local, regional, and global atmosphere. The main gases produced during BB include carbon dioxide (CO_2), carbon monoxide (CO), methane (CH_4), and nitrogen oxides (NOx). CO, CH_4, and NOx lead to the photochemical production of ozone (O_3) in the troposphere that can be really harmful at high concentrations [13]. Several studies have documented O_3 formation in smoke plumes [14,15], while others have suggested that wildfires lead to an increased amount of ground-level O_3 [15,16]. For instance, wildfire emissions are reported to enhance the average summertime monthly mean of O_3 concentration by 2–8 ppb [17,18], while other studies have shown that the observed O_3 to CO enhancements in smoke plumes attributed 3.5% of the global tropospheric O_3 production to BB emissions [19,20].

The record-breaking bushfires in southeast Australia in the summer of 2019–2020 were the most devastating in the history of the country. According to Filkov et al. (2020) [21], almost 19 million hectares were burned and more than 3 thousand houses were destroyed, while 33 people and more than 1 billion animals were killed, causing extreme damage to the wildlife and the ecosystem. The meteorological conditions were very favorable for the wildfire ignition and spread, increasing the severity of the event. The recorded temperatures were extremely high (+1.33 °C of the mean temperature and +1.59 °C of the local mean maximum) and the resulting drought was intense (annual mean precipitation of 277.6 mm) [21].

These extreme wildfires occurred within the midlatitude cyclones belt [22], at relatively south latitudes where the tropopause height (TPPH) is relatively low. Along with the strong pyrocumulonimbus (pyroCB) convection [23], the emitted BB aerosols managed to reach the higher troposphere and enter into the stratosphere. Compared to a similar extreme event of the North Hemisphere in 2017 (Pacific Northwest Wildfire Event) that injected about 0.1–0.3 Tg of smoke particles into the stratosphere [12,24,25], the impact from the Australian brushfires (2019–2020) was much larger and injected the record amount of 0.4 ± 0.2 Tg in the stratosphere [5,23,26].
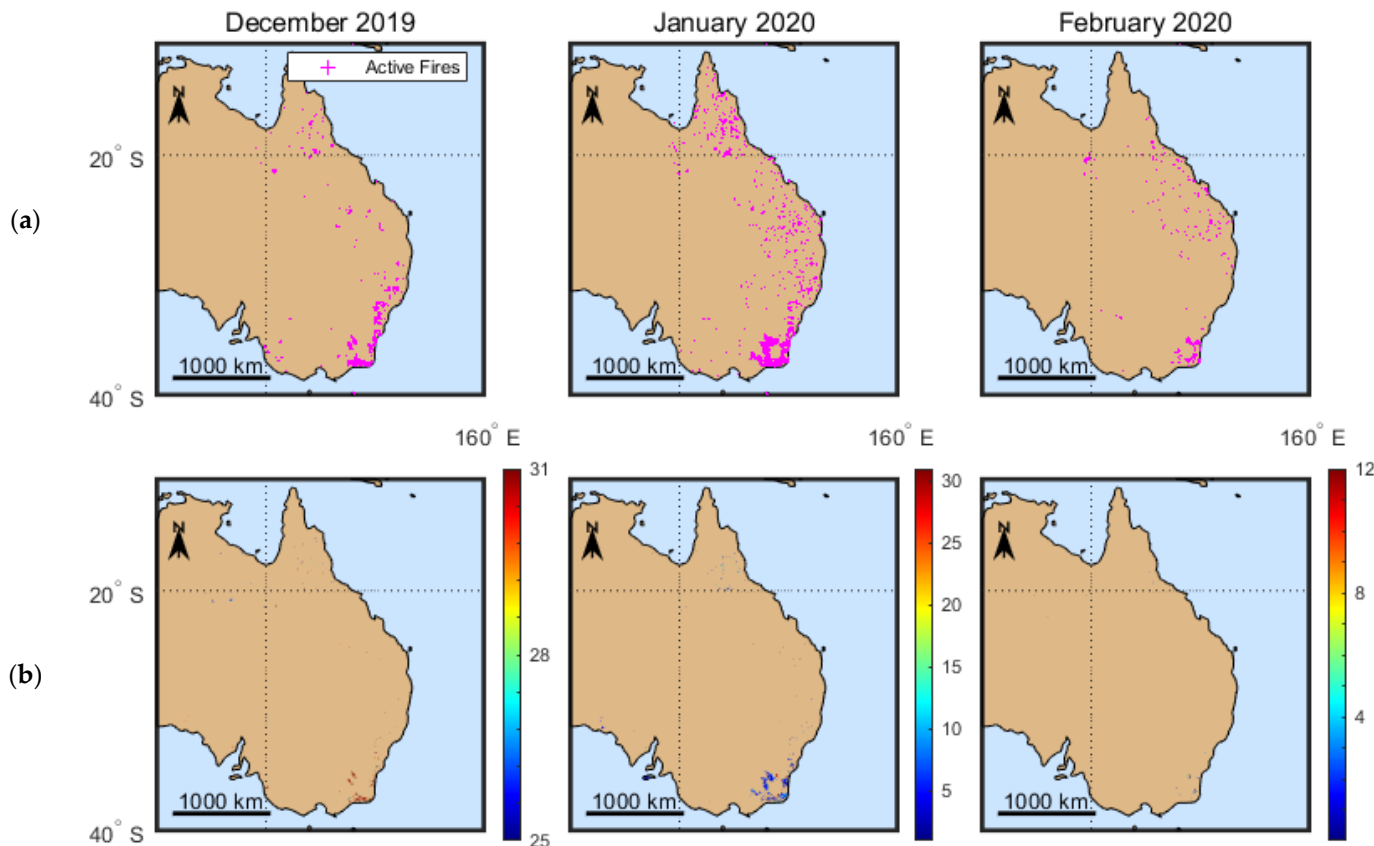
To date, an important number of studies have already investigated the event of the 2019–2020 Australian bushfires in terms of the aerosol optical, chemical, and radiative properties [3–6,27–30]. These studies either focus on specific regions/sites [4,30], or they utilize mostly passive remote-sensing techniques, without any information on the vertical distribution of aerosol properties. Here, we study this extreme event over an extended time span (from 25 December 2019 to 12 February 2020), using range-resolved aerosol measurements by the Cloud-Aerosol Lidar with Orthogonal Polarization (CALIOP) spaceborne lidar instrument. Moreover, concentrations of CO and O_3 are also studied, as they are obtained by the Copernicus Atmosphere Monitoring Service (CAMS) at various pressure levels. In order to investigate the effect of the BB plume on a greater horizontal area, we recorded all the smoke layers and chemical concentrations extending from Australia (140° East) to the east coasts of South America (20° West), and within a latitude range of 20°–60° South. Dispersion simulations with a FLEXPART model were also used to support the aerosol observations and describe the atmospheric motions. The smoke layers were

analyzed in terms of their geometrical and optical properties. To understand the radiative effect of the event, indicative cases of tropospheric and stratospheric smoke layers were used for analyzing the radiative forcing (RF) of BB particles.

2. Methods and Tools

2.1. Moderate-Resolution Imaging Spectroradiometer (MODIS): Active Fire Data and Burned Area Product

We used satellite products from the MODIS instrument, onboard the Terra and Aqua platforms, to analyze the distribution of active fires and burned area in Australia. The active fire data and MODIS burned area product are distributed through the Fire Information for Resource Management System (FIRMS: https://firms.modaps.eosdis.nasa.gov, last accessed: 10 January 2022) and through https://lpdaac.usgs.gov/products/mcd64a1v006/ MCD64Al: (last accessed: 26 January 2022), respectively. The use of these data permitted us to locate and emphasize the exact area and period of fires. Figure 1 shows the locations at which MODIS detected at least one fire event [31,32] during the compositing time period, with confidence greater than 70% (magenta crosses). The different colors of the burned area map correspond to different burn dates, starting from December 2019 to February 2020.

Figure 1. (**a**) Active fires and (**b**) burned area according to burn date, as obtained by MODIS for the time period of 25 December 2019–12 February 2020.

As shown in Figure 1a, during the study period (25 December 2019–12 February 2020), active fires spread all over the eastern coasts of Australia. Most of the active fires were located at the southeastern (New South Wales, NSW, and Victoria) and the northeastern (Queensland) parts of the country. The southeastern part, especially the area close to the borders of NSW and Victoria (~37° S, ~150° E), was highly affected by the fires. The areas burned from these bushfires (Figure 1b), were mostly burned during the last few days in December and the first few days in January, while a confined area was also burned during the first few days in February.

2.2. CAMS Reanalysis Data on Different Pressure Levels

The Copernicus Atmosphere Monitoring Service (CAMS; http://atmosphere.copernicus.eu, last accessed: 8 February 2022) is a component of the European Earth Observation program Copernicus. The CAMS global near-real-time service provides daily analyses and forecasts of reactive trace gases, greenhouse gases, and aerosol concentrations. CAMS reanalysis is the latest global reanalysis dataset of atmospheric composition produced by the European Centre for Medium-Range Weather Forecasts (ECMWF), consisting of three-dimensional time-consistent atmospheric composition fields, including aerosols and chemical species [33]. The dataset covers the period 2003–2021. The atmospheric products can be found on single levels, total column, model levels, and pressure levels. Different pressure levels covered the vertical range from 1000 to 1 hPa within 25 layers, with a horizontal resolution of 0.75° × 0.75°, and a temporal resolution of 3 h. In this study, the mass mixing ratio of CO (kg/kg) and O_3 (kg/kg) [34] was used on the pressure levels 950–200 hPa to find the enhancement of O_3 relative to CO in the smoke plumes.
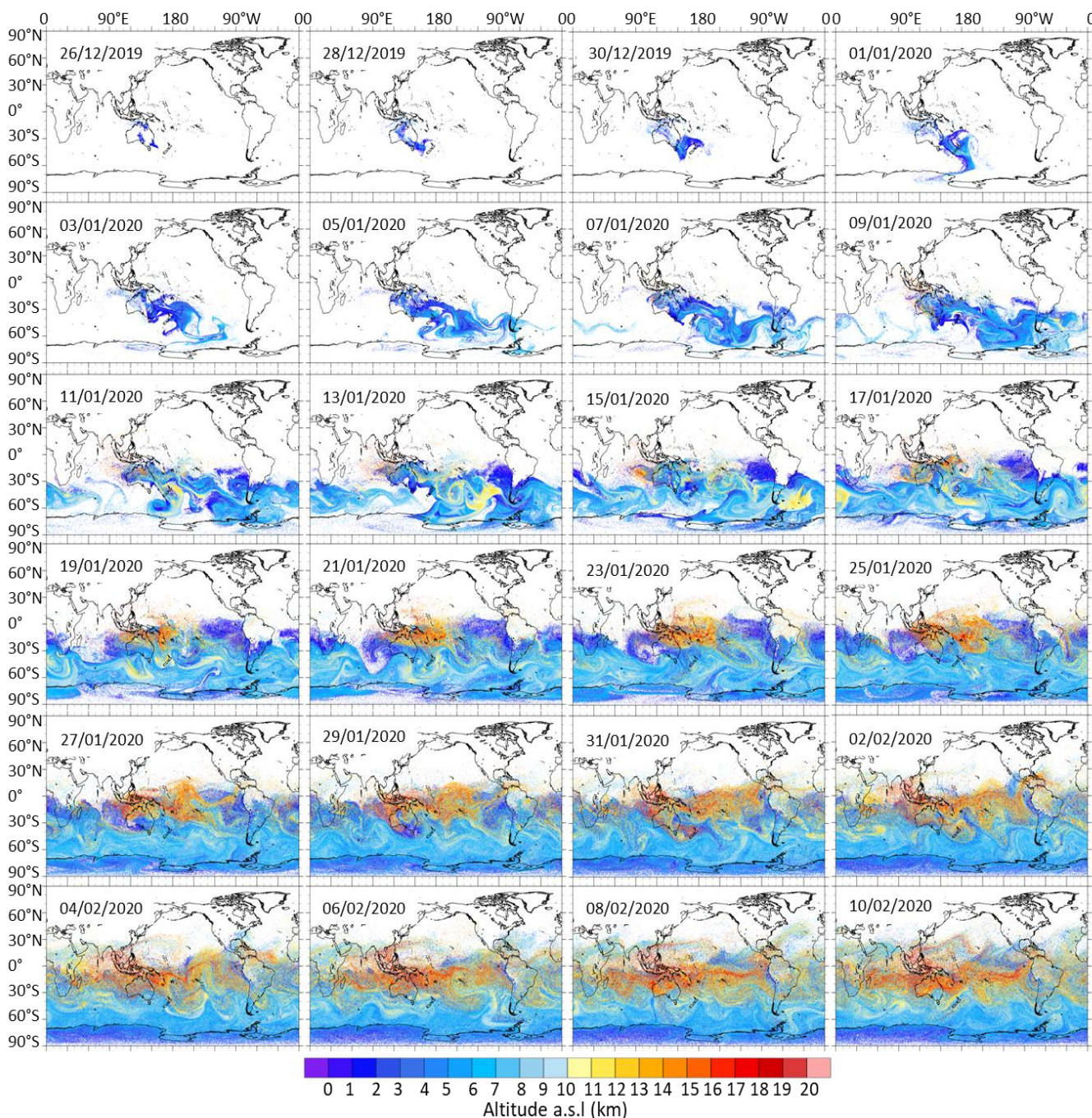
2.3. FLEXPART Model

We used the Lagrangian transport model FLEXPART (FLEXible PARTicle) to simulate the forward dispersion of smoke particles from the wildfires [35,36]. The simulations were initialized from the MODIS hot-spot detections and the meteorological driver was the 6-hourly final analysis dataset (FNL) from the National Centers for Environmental Prediction (NCEP) at 1° × 1° resolution. The emitted particles were assumed to be black carbon (BC) and 1000 particles were attributed to each emission. Dry deposition as well as in-cloud and below-cloud scavenging were enabled for these runs. In order to limit our analysis only to the fires that actually contributed to the long-range transport of smoke, we excluded all hot spots with fire radiative power (FRP) less than 1000 MW, resulting in a total of 1611 emissions. The injection height for each emission was parameterized based on the observed FRP as similar to Solomos et al., 2019 [37]:

$$INJ_{\text{HGT}}(\text{m}) = 10^{0.39 \times \log_{10}(\text{FRP})+2)} \tag{1}$$

This approach is computationally efficient and provides a physically based distribution of injection heights for mid-latitude fires.

As can be observed in Figure 2, the meteorological conditions during the study period result in a complex dispersion pattern for the simulated smoke particles over the entire southern hemisphere. The suspended particles are elevated to altitudes above 10 km as they travel eastwards from Australia towards South America, favored by the mesoscale circulation patterns in the South Pacific Ocean. After 17 January 2020, large portions of the plumes are found above a 15 km height, especially over the northeast parts of Australia. Until 10 February 2020, a distinct latitudinal belt of elevated smoke up to stratospheric levels is evident between the Equator and 30° S.
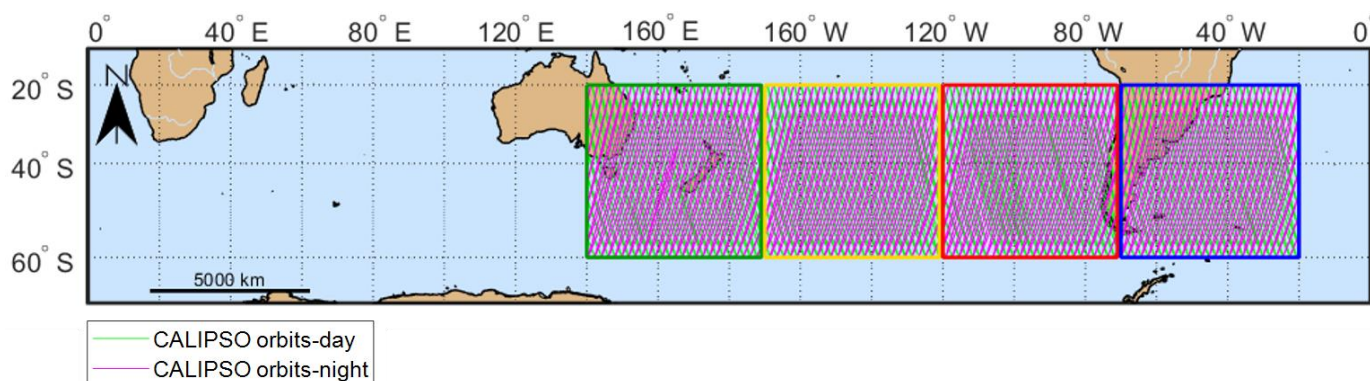
Figure 2. Biomass burning aerosol's height, as calculated by the FLEXPART model for the under-study period (25 December 2019–12 February 2020).

2.4. The Cloud-Aerosol Lidar and Infrared Pathfinder Satellite Observation (CALIPSO) Satellite

The CALIOP elastic backscatter lidar system is onboard the CALIPSO polar-orbiting satellite, flying at an altitude of about 705 km, with a laser footprint covering 0.2% of the Earth's surface during one full cycle. CALIOP emits simultaneously at 532 and 1064 nm (https://www-calipso.larc.nasa.gov/, last accessed: 16 February 2022). It has provided vertically resolved aerosol and cloud properties on a global scale [38] since 2006, offering substantial research advantages in aerosol and cloud studies [39]. In this work, the L2 version 4.20 CALIPSO Aerosol Profile (APro) and the Vertical Feature Mask (VFM) data products were used, which are provided with a 5 km horizontal resolution. From the Apro products, the extensive and intensive aerosol optical properties are derived, namely,

the aerosol backscatter coefficient (b_{aer}); the extinction coefficient (a_{aer}); the particle linear depolarization ratio (PLDR) at 532 nm; Ångström exponent, related to the backscatter coefficients obtained by the pair of wavelengths 532 and 1064 nm ($Å_b$); as well as the aerosol optical depth (AOD; calculated by the integration of the a_{aer} over the smoke layers). The VFM products were used for separating aerosols from clouds, and further classifying aerosols in various types [40], in order to keep the ones related to BB aerosols, namely, types 3 (polluted continental/smoke; top of the layer lower than 2.5 km) and 6 (smoke; top of the layer higher than 2.5 km), as classified by the CALIPSO algorithm. CALIOP's aerosol lidar ratio is determined for each aerosol subtype based on measurements, modeling, and the cluster analysis of a multiyear Aerosol Robotic Network (AERONET) dataset [40]. Each aerosol type is associated with a lidar ratio, which allows the calculation of aerosol extinction coefficient from the attenuated backscatter [41]. Omar et al. (2009) [40] indicated that a maximum uncertainty of 30% is associated with the determination of lidar ratios. A significant underestimate of aerosol extinction in clean regions is also possible [42], while CALIOP could also misclassify low aerosol concentrations as clear air when no aerosol is detected due to the CALIOP detection threshold. A recent study [43] also showed a misclassification between smoke and sulphate aerosol layers. Moreover, large differences also exist between day- and night-time measurements, while the decreased signal-to-noise ratio during daytime affects the detection of low aerosol extinction values [44].

　　　Nevertheless, the CALIPSO satellite offers a unique opportunity to study such dynamic events, such as the one analyzed in this study, from their source region and across the intercontinental path that aerosols follow, where no ground-based lidars exist [45]. Thus, in this study, it was used to track all the BB aerosol plumes as they were transported from Australia to South America. In order to detect any possible change in the geometrical and optical properties of the smoke layers, the main region of smoke's spatial distribution was limited from 20° S to 60° S. Within this latitude range, four study regions were created, the green (GR), yellow (YR), red (RR), and blue (BR) one, starting from the source of the fires in Australia (GR) and ending just after the South American continent (BR). All regions were located between 140° E and 20° W, with the exact same longitude range of 50° (Figure 3). The GR region surrounds the active fire area and the CALIPSO orbits closest to this area, containing freshly emitted smoke particles. Each one of the other regions was originated, so that the smoke layers in each transportation phase towards the South America would be captured.

Figure 3. CALIPSO day- and night-time orbits per region of study, for the time period of 25 December 2019–12 February 2020.

　　　All the night-time and daytime CALIPSO orbits above each study region were used to obtain as much information as possible about the event. The retrievals were obtained per 2° latitude and longitude, along each CALIPSO orbit. Profiles that did not contain any smoke layers were excluded from our statistical analysis. However, most of them included more than one smoke layer at different altitude levels, both in the troposphere and stratosphere. A horizontal averaging of 105 km was applied to the CALIOP data to

enhance the detection of the aerosol layers and increase the signal-to-noise ratio of the profiles. The data were screened using standard CALIPSO quality-assurance flags and cloud aerosol discrimination (CAD) scores [39,42]. At this point, it is worth mentioning that, since September 2016, CALIOP has been experiencing low-laser-energy shots, which mostly occur over the South Atlantic Anomaly (SAA) region. As of March 2018, ~6% of all laser shots within the SAA have low energy, whereas the global frequency remains less than 1% [46]. This fact may have affected the number of layers at the fourth study region (BR).

The smoke layers analyzed in this study were selected based on the aerosol typing algorithm, but also extra limitations were applied to them. More precisely, tropospheric aerosol layers had to be of thicknesses greater than 500 m, while no aerosol thickness limitation was applied to the stratospheric ones. Regarding the aerosol optical properties, only smoke layers with b_{aer} and PLDR values above 0.1 $Mm^{-1}sr^{-1}$ and 0.01 were kept, respectively. These two values were set as a threshold, in order to make sure that only valid aerosol layers were kept for further processing in our analysis. More precisely, the threshold value of 0.1 $Mm^{-1}sr^{-1}$ for the backscatter coefficient was set in accordance to the attenuated aerosol backscatter detectability limit of CALIOP, which has been reported to be of the order of 10^{-1} $Mm^{-1}sr^{-1}$ [47,48]. Additionally, the threshold value regarding PLDR observations was set to be 0.01, a value very close to the molecular depolarization values (~0.8% [49], depending on the wavelength and the atmospheric conditions [50,51], as PLDR values lower than that cannot be found in the literature concerning aerosol layers. Our approach, apart from ensuring that no misclassified aerosol layers were included in our analysis, due to their small backscatter coefficient or small PLDR values, also excluded any possible layers obtained over SAA, due to low-laser-energies.

2.5. The Libradtran Radiative Transfer Model

For estimating the radiative effect of this BB event, a variety of cases was selected from each studied region based on the magnitude of the AOD. We ended up with five tropospheric and five stratospheric layers from each region. A total of 44 vertical levels were considered from the surface up to a 70 km height. Starting from the ground level (surface; SRF) and up to 20 km, the vertical resolution was 0.5 km, while the corresponding one from 20 to 70 km (top of the atmosphere; TOA) was 20 km. The a_{aer} profiles at 532 nm obtained from the CALIOP measurements for each smoke layer were used as inputs in the LibRadtran radiative transfer model version 2.0.2. [52]. In our study, the uvspec algorithm, which calculates the radiation field in the Earth's atmosphere, was implemented for the disort radiative transfer equation (1-D geometry) for the downwelling and upwelling shortwave (SW, 280–3000 nm) and longwave (LW, 3000–30,000 nm) irradiances. Midlatitude summer conditions were used for a typical Air Force Geophysics Laboratory (AFGL) Atmospheric Constituent Profile [53], along with a surface albedo value of 0.06 for the ocean areas and 0.20 for the land areas in the SW range that were considered. For each case, two simulations (one for the SW and one for the LW range) referred to clear-sky atmosphere with background aerosol conditions and two simulations corresponded to the smoke-loaded atmosphere, since SW and LW ranges were treated separately by LibRadtran. The aerosol RF depicts the perturbation in flux in the atmosphere caused by the presence of the aerosol layers in relation to that calculated under clear-sky conditions [54,55], and it is given by:

$$RF(z) = \Delta F_{smoke}(z) - \Delta F_{clear}(z) \tag{2}$$

where ΔF, at level z, is calculated by:

$$\Delta F(z) = F{\downarrow}(z) - F{\uparrow}(z) \tag{3}$$

$F{\downarrow}(z)$ and $F{\uparrow}(z)$ are the downwelling and upwelling fluxes.
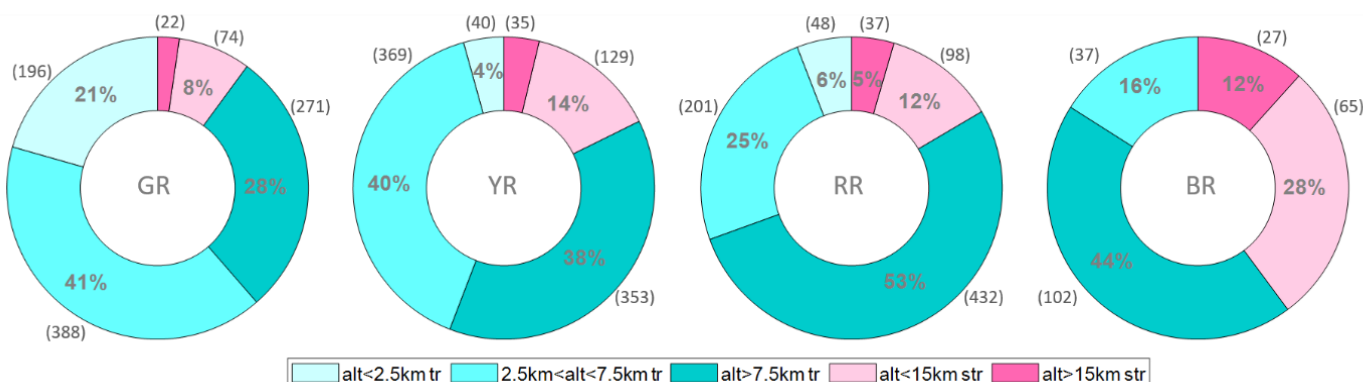Therefore, the net RF, $RF_{NET}(z)$, is expressed by:

$$RF_{NET}(z) = RF_{SW}(z) + RF_{LW}(z) \tag{4}$$

It is important to notice that these estimations did not take the presence of clouds into account. For a typical average cloud coverage over the area, the surface all-sky RF can be reduced to ~50% and the TOA all-sky RF to ~30–50% of the clear-sky RF estimations [5]. Finally, since the under-study cases referred to different days, times, and coordinates, the solar zenith angle (SZA) ranged between 24.65° and 46.86°.
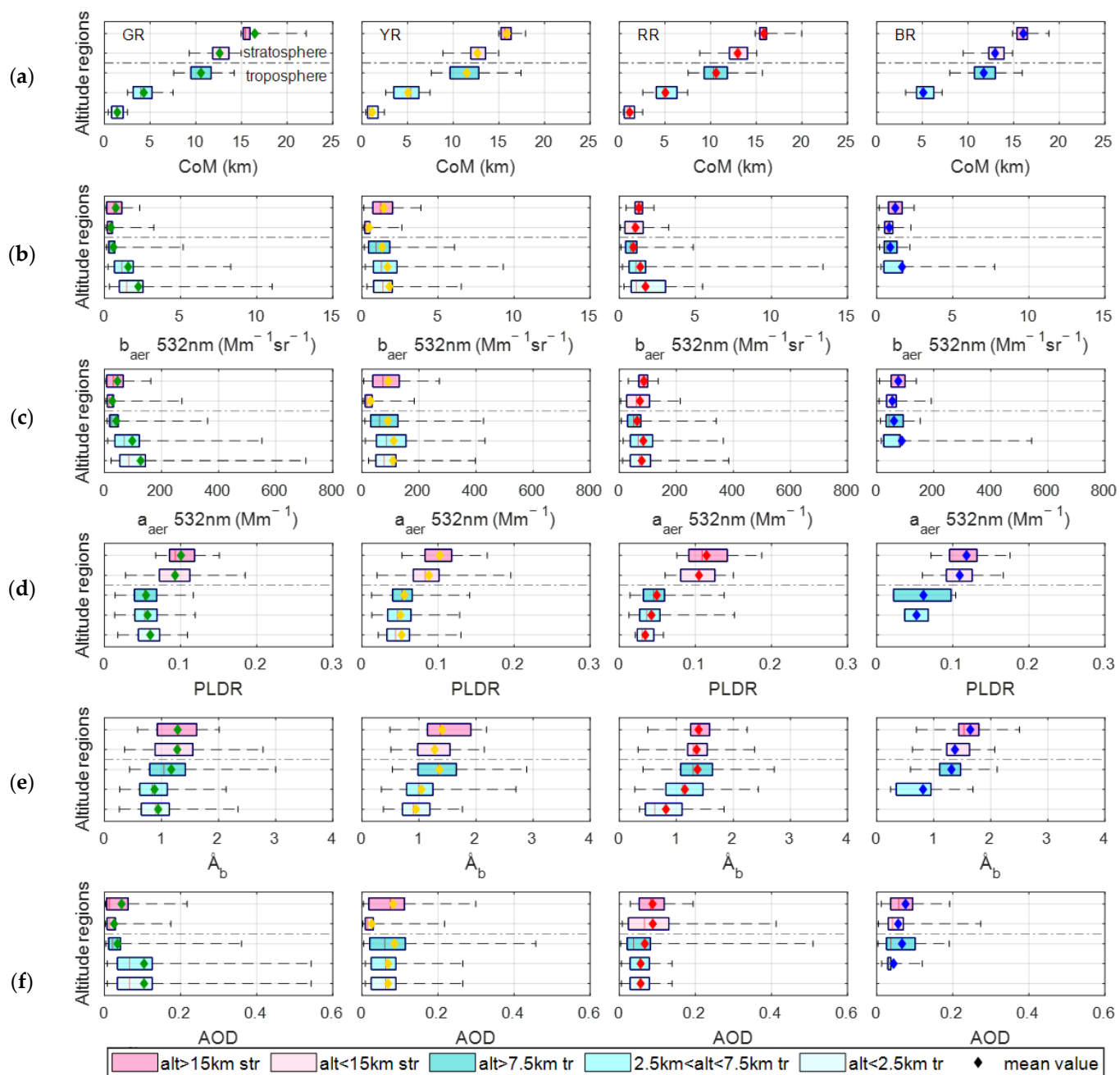
3. Results and Discussion

3.1. Aerosol Geometrical and Optical Properties per Study Region

For the time period from 25 December 2019 to 12 February 2020, the day and night CALIPSO orbits were used, and the aerosol vertical profiles were retrieved per 2° lat., covering the entire under-study region (20° to 60° S and 140° E to 20° W). As mentioned in Section 2.4, only the aerosol layers that were categorized as types 3 and 6 based on CALIPSO Level 2 v4.20 algorithm were kept and further analyzed. The total number of the selected BB aerosol layers, accumulated over time and space, was 3124 (GR: 1151, YR: 926, RR: 816, and BR: 231 BB layers). In order to study the vertical structure of the plumes in this admittedly large time–space scale, we divided the observed BB layers into 5 altitude-range categories (3 tropospheric and 2 stratospheric), according to their mean height range extensions. The first tropospheric category contained layers below 2.5 km amsl., the second contained layers observed within 2.5 to 7.5 km amsl., while layers observed above 7.5 km amsl. and reaching up to the TPPH were finally grouped in the third tropospheric category. On the other hand, the two stratospheric groups of layers were associated with aerosol layers observed between TPPH and 15 km amsl., and with layers above the 15 km amsl. The percentages of the layers found within each altitude category and region are extensively shown in the following diagrams (Figure 4).

Figure 4. Percentages of BB aerosol layers found in each under-study region (from left to right: GR, YR, RR, and BR) and altitude category (chromatic scale). The numbers shown in the parenthesis next to the percentages refer to the accumulated actual number of observed layers.

Furthermore, in order to obtain representative (for each region and for each altitude-range category) values of the aerosol properties, namely, the b_{aer}, a_{aer}, PLDR (at 532 nm), $Å_b$ (532/1064 nm), and AOD (at 532 nm), we proceeded with the box-plot analysis presented in Figure 5. This analysis provides information about the distribution of the aerosol properties values previously mentioned, for all the smoke layers studied during the event. Boxes of cyan-color shades correspond to tropospheric and light and dark pink shades to stratospheric layers. The rhombus symbol, of different colors for each region, represent the mean value of each property. The horizontal line inside the boxes refers to the median values, while the min. and max. values are indicated at the end of the whiskers. The box limits correspond to the 75th and 25th percentile values of the dataset.

Figure 5. BB aerosol layers according to (**a**) their CoM (amsl.), (**b**) b_{aer}, (**c**) a_{aer}, (**d**) PLDR at 532 nm, (**e**) $\mathring{A}_b$ (532/1064 nm), and (**f**) AOD at 532 nm. GR, YR, RR, and BR (left to right) correspond to the four under-study regions, while the different colors indicate the different height-range categories.

The center of mass (CoM) of the smoke layers was calculated according to Mona et al. [56] per study and altitude region (Figure 5a) to find the vertical spread of the aerosols in the atmosphere. Smoke layers were identified in all 4 regions, extending from the ground up to 22 km amsl., except for the BR, for which no smoke layers were found in the lower height-range group. This fact could possibly be connected to the SAA effect, as mentioned in Section 2.4. Specifically, the tropospheric BB aerosol layers were found from near 0.5 km reaching altitudes up to 14.20 km in the GR, 17.42 km in the YR, 15.69 km in the RR, and from 3.18 to 15.94 km in the BR. The mean CoM of the stratospheric layers were found to be around 16 km in all the regions, with higher variabilities (9.29–22.09 km) to be observed in the region containing the active fires (GR).

In general, the b_{aer} and a_{aer} values, retrieved from each layer, decreased with the altitude, presenting higher values in the tropospheric altitude-range categories (Figure 5b,c). In the GR, mean values of b_{aer} ranged from 0.59 ± 0.63 to 2.23 ± 2.10 Mm^{-1}sr^{-1}. In YR, the corresponding mean values were found to be between 1.33 ± 1.16 and 1.81 ± 1.59 Mm^{-1}sr^{-1}, while, in RR, the b_{aer} values ranged from 0.93 ± 0.65 to 1.72 ± 1.31 Mm^{-1}sr^{-1}, even reaching the extreme value of 13.39 Mm^{-1}sr^{-1} in the lower free troposphere (FT; alt. < 7.5 km). In BR, the b_{aer} values ranged from 0.89 ± 1.66 to 1.67 ± 1.86 Mm^{-1}sr^{-1}. The relatively low recorded values close to the fire region could be related to the fact that CALIOP is a nadir-only looking lidar, therefore the data were only collected along the satellite's orbit, and thus there is a possibility that some smoke plumes were not found at the exact overpass time and/or coordinates of the satellite track. However, considering the fact that, in our study, the statistical sample was very high, such uncertainties were probably eliminated and the main reason behind these decreased values was the high averaging areas over each grid that wiped out any detailed information that could be observed.

Additionally, the Andes mountain range could have played a role in this increase (FT b_{aer} values in the RR), as well as in the decrease in the number of layers in the BR. In particular, the narrow and steep Andes mountains act as a physical barrier to the Pacific Ocean FT [57]; they significantly disturb the atmospheric circulation resulting in a variety of synoptic and meso-scale phenomena, as well as climate conditions of sharp contrast between tropical and subtropical latitudes, along with a pressure-longitude cross section of the seasonal mean zonal wind summertime circulation [58], in which the aerosols are trapped within the RR. The aerosols uplift along the slopes of the mountains and then dive again into the Pacific, staying for longer time periods in the RR and possibly mix with other smoke layers not being able to move easterly, towards the BR.

The b_{aer} stratospheric values were found to be lower than the tropospheric ones, for all regions, ranging between 0.42 ± 0.40 and 1.44 ± 0.99 Mm^{-1}sr^{-1}. In contrast, the tropospheric a_{aer} values were greater than the stratospheric, in all regions, ranging from 41.26 ± 43.74 to 126.63 ± 117.88 Mm^{-1}, with a maximum recorded value of 705.78 Mm^{-1} observed at the lower tropospheric category (<2.5 km) in GR, apparently influenced by the emissions at the ground. In the rest of the regions, the values were found between 60.68 ± 34.21 and 111.52 ± 83.06 Mm^{-1}. The maximum recorded values of b_{aer} show a descending trend, except for the BR in which a maximum value of 542.94 Mm^{-1} appeared in the lower FT, which could also be related to smoke layers from the same event or even layers originating from fires in South America, active at the same time period (Figure A1), which may, additionally, have contributed to the smoke layers transported from Australia. In the stratosphere, the a_{aer} values ranged from 27.14 ± 32.41 to 92.59 ± 95.08 Mm^{-1}, while a maximum recorded value was 271.38 Mm^{-1}. In general, both a_{aer} and b_{aer} seem to have a descending trend in the troposphere as the smoke moved westerly, passing over the four regions, while, for the stratospheric layers, it appears to be the exact opposite (Figure 5b,c). These b_{aer} and a_{aer} values, both in tropospheric and stratospheric heights, point out the significant impact of the event on the atmosphere at an almost hemispheric scale. Moreover, the PLDR values increase with altitude in each region (Figure 5d). In the troposphere, the corresponding mean values were lower than 0.06, showing the presence of nearly spherical particles in the smoke layers, indicative of BB mixed with aerosols of sea-spray-origin [45,59,60]. The maximum tropospheric PLDR values did not exceed 0.15, while, in the stratosphere, values as high as 0.20 were observed. Since high PLDR values suggest particles of irregular solid shapes, our stratospheric observations could possibly indicate that the smoke particles acquired an ice coating at the colder stratospheric temperatures, consistent with the ice-nucleating potential of smoke particles [61,62]. Similar values of PLDR have been reported by two recent publications addressing the same event of BB aerosol plumes observed over Chile by a depolarization lidar (~0.20) [4] and over the French Antarctic Station (0.07–0.13) [30]. In a good agreement with our results were, also, the PLDR values reported by studies concerning stratospheric smoke in the Northern Hemisphere originating from Canadian wildfires [2,11,12]. The presented PLDR values

repeated the same pattern (lower values in the three tropospheric altitude-range categories and higher in the two stratospheric ones) over all regions. A slight decrease in tropospheric PLDR values was observed, as the smoke moved westerly, across the South Pacific Ocean, indicating that the tropospheric aerosols were becoming even more spherical, probably due to the increased relative humidity that affected them as they were transported over the ocean [63,64]. In contrast, the stratospheric aerosols tended to be less spherical (Figure 5d), probably because of their ice-nucleating potential already mentioned above.

Fine and ultrafine smoke particles were dominant in the stratosphere, since the observed $Å_b$ values were found to be relatively high, reaching even up to 3 in the first two regions (GR, YR). On the other hand, $Å_b$ values in the troposphere found to be below 1 (min. down to 0.27 in lower atmosphere), indicating coarser particles, possibly BB mixed with marine aerosol (Figure 5e). As the tropospheric aerosols moved towards North America, a slightly descending trend was observed, showing that they had probably grown in size as they fended off the source, while the stratospheric $Å_b$ values were slightly increased (Figure 5e).

Concerning the smoke load represented by the AOD values shown in Figure 5f, it is evident that higher loads are recorded in the lower troposphere, compared to those of the upper atmosphere, something that could be related both to the thickness of the tropospheric layers and their opacity. The maximum AOD value of 0.54 was recorded in the lower troposphere over the fire spots (GR), while in the stratosphere AOD values reached up to 0.29, similar to the values (0.05–0.33) observed in the stratosphere over Chile [4].
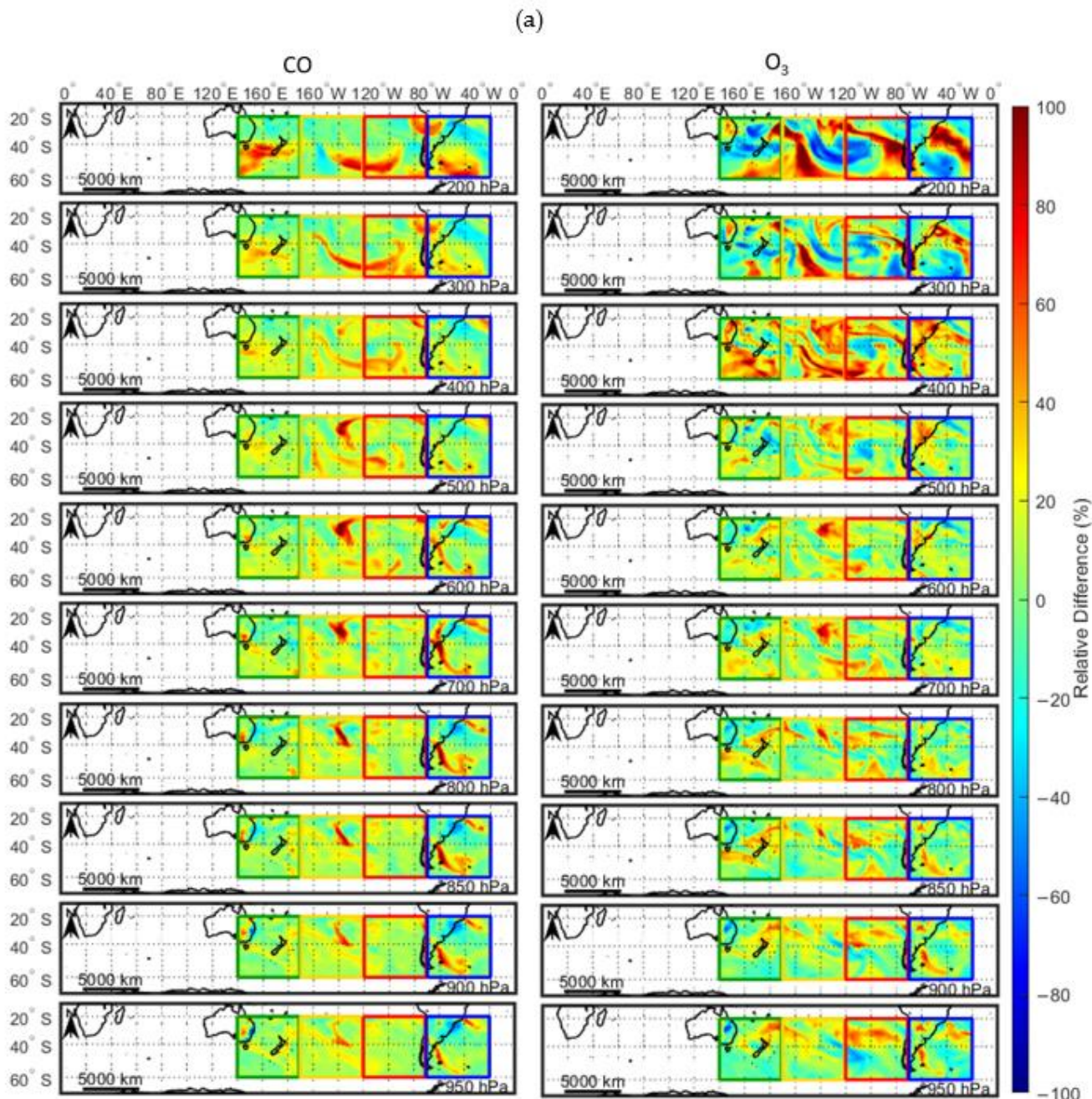
Relevant studies addressing the same event by utilizing mostly passive remote-sensing techniques over Australia showed $Å_b$ values of ~1.5 [27] and AOD values in a range of 0.15 to 2.76 [1,27,28]. The measured values, as obtained by MODIS and/or AERONET over the fire region at wavelengths 440 and 550 nm, were in a good agreement with our results over GR, considering the lack of any information of the vertical distribution. Differences between the maximum observed AOD values (~2.76) could be explained by the fact that these values refer to the total atmospheric column, while our corresponding results (max 0.54) refer to distinct aerosol layers.

3.2. Chemical Properties: CO and O_3 Variations over the Study Area
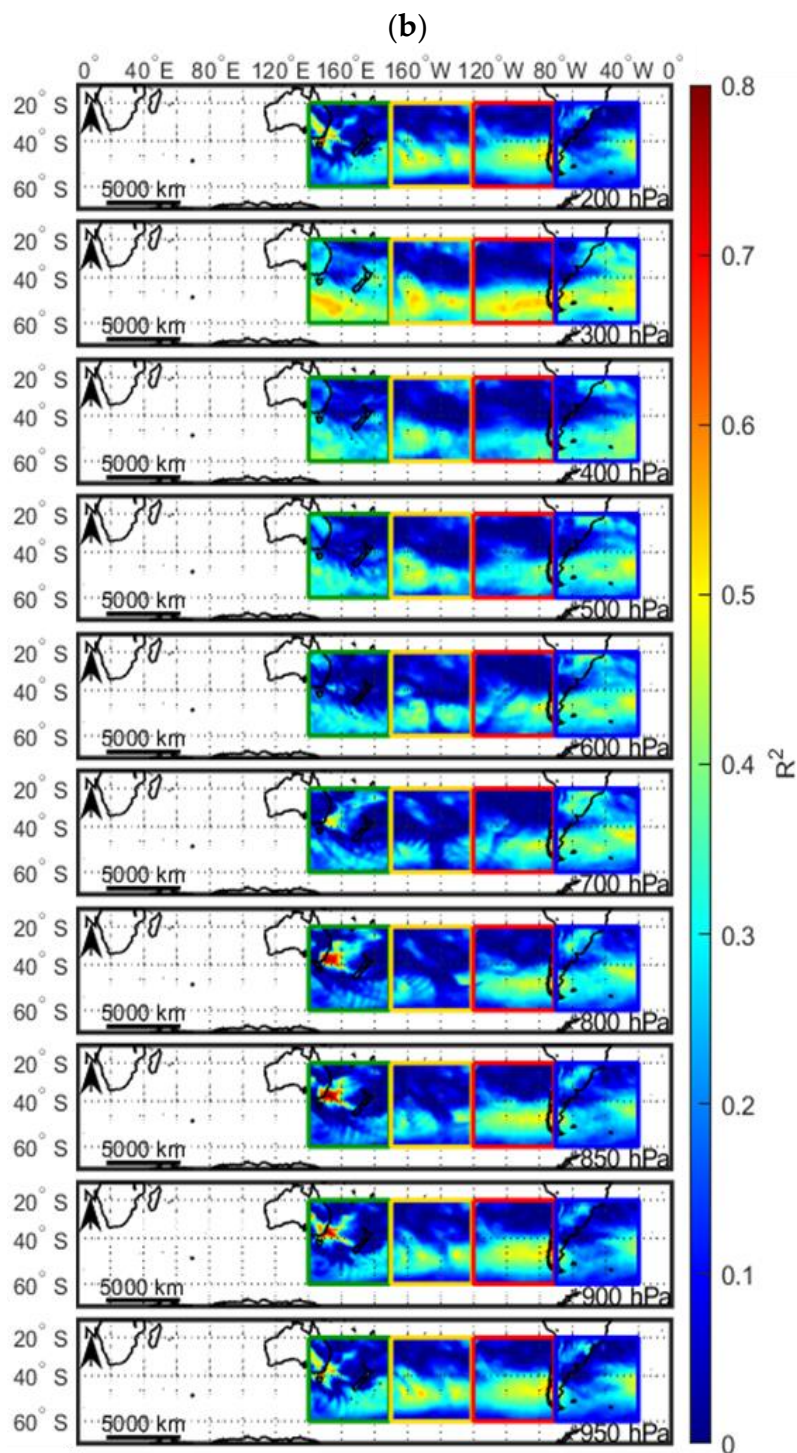
Apart from a major source of atmospheric aerosols, BB is also a great source of trace gases that can significantly impact atmospheric chemistry, climate forcing, as well as air quality and human health [19]. Wildfire smoke is an important source of CO, NOx, and VOCs, emitted directly into the atmosphere, and may additionally contribute in tropospheric O_3 formation through photochemistry during fire seasons [15,19,20]. For that reason, we calculated the relative changes of the CO and O_3 for the entire time period of our study (25 December 2019–12 February 2020), with respect to the corresponding days of the months for December and January, but for the last 15 years (base period: 2004–2019). This analysis was performed for the same region as of our aerosol optical properties study (20° to 60° S and 140° E to 20° W), and the results are shown in Figure 6a,b. During the above-mentioned time period, the CO concentration was found to increase up to 100%, compared to the base period, mostly in the higher-pressure levels (700–950 hPa) of the three last regions (YR, RR, BR). In the GR, the highest observed increase in CO was 92% at 950 hPa. Correspondingly, the O_3 enhancement presented values of 60–96% in the lower atmosphere and even 100% in the upper one (pressure levels 200–400 hPa). The mean values and standard deviations (std) of CO and O_3 concentrations relative change per region are presented in Table A1.

In order to investigate the impact of emitted CO on the O_3 formation, we calculated the correlation coefficient (R^2) between the relative change concentrations of the aforementioned gases during the study period (6 h temporal resolution), with respect to the base period (Figure 6b). A significant correlation (R^2~0.8) was revealed between CO and O_3 during the study period in most of the pressure levels, especially close to the fire source (GR). For the rest of the regions, moderate values of R^2 were found (0.4–0.6), suggesting

that the CO variation did not play a key role in the observed O_3 enhancement. Some grids showed higher O_3 enhancement relative to CO (0.5–0.8), while others showed lower (0–0.4). However, increased chemical processes were expected to occur to an aerosol layer with a longer lifetime and wider transportation in the atmosphere, and hence a greater possibility of O_3 production [65], although this may have been affected by various other parameters, such as solar radiation and/or atmospheric temperature [66]. When trying to study these changes with respect to the day- and night-time conditions (Figure A2), we found that the correlation coefficient did not vary significantly, indicating that the variation of solar radiation played a minor role in the presented anomalies, and the latter can be attributed mostly to the event itself.

Figure 6. *Cont.*

Figure 6. (**a**) Relative differences of CO and O$_3$ calculated for the study period (25 December 2019 to 12 February 2020) over the study area (20° to 60° S and 140° E to 20° W), with respect to the same days through the years 2004–2019 (base period). (**b**) R^2 between CO and O$_3$ relative differences with respect to the base dataset, at various pressure levels (950–200 hPa).

3.3. Radiative Forcing of the Event

In order to estimate the role of the fire-emitted BB aerosols in the Earth's radiation budget, we performed simulations to quantify their impact on the radiative forcing. The mean RF$_{NET}$ at the TOA, within the smoke layers and at the SRF-level was calculated during our simulations, using the LibRadtran radiation code twice: one for the index "clear", and

one for the index "smoke" (Equation (1), Section 2.5). The latter includes the presence of the free tropospheric and stratospheric BB aerosol layers, so that the contribution of the BB load in the RF_{NET} (with respect to the "clear") could be found.
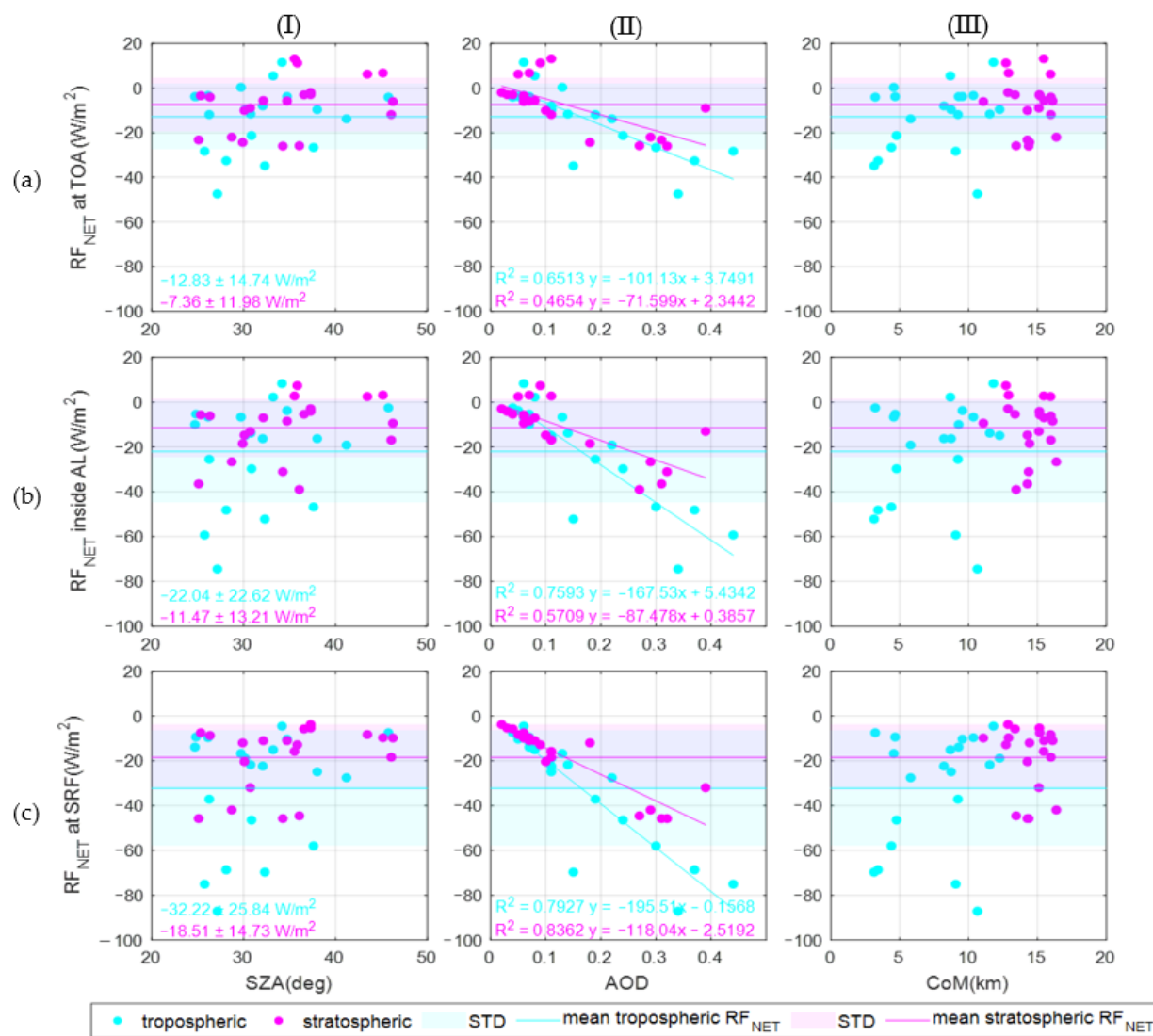
The RF_{NET} of each aerosol layer observed in the entire under-study region is presented in Figure 7. The calculated RF_{NET} values, for a range of the SZA between 24.65° and 46.86°, was found to vary from −87.10 to +13.18 W/m^2 (Figure 7I(a–c)), indicating cooling and heating, respectively. At the TOA, it ranged from −47.42 to +11.56 W/m^2 (mean value −12.83 ± 14.74 W/m^2) for the tropospheric aerosols, and from −25.96 to +13.18 W/m^2 (mean value +7.36 ± 11.98 W/m^2) for the stratospheric ones. Inside the tropospheric aerosol layers, the RF_{NET} was found between −74.47 and +8.30 W/m^2, with a mean value equal to −22.04 ± 22.62 W/m^2, while, inside the stratospheric layers, it was found between −38.99 and +7.40 W/m^2, with a corresponding mean value equal to −11.47 ± 13.21 W/m^2. At the SRF, the corresponding ranges were −87.10 to −4.53 W/m^2 for the tropospheric layers, and −45.79 to −3.80 W/m^2 for the stratospheric ones. The mean values were found to be equal to −32.22 ± 25.84 W/m^2 and −18.51 ± 14.73 W/m^2, respectively.

From (Figure 7I(a–c)), there is no evidence of SZA dependency with RF_{NET}, since the presented values do not follow any specific pattern concerning the SZA ranges, probably because of the SZA narrow range of variation. However, according to the slopes of the regression lines and the R^2 values, the RF_{NET} seem to have a good correlation with the aerosol load (Figure 7II(a–c)). More precisely, the correlation between RF_{NET} and AOD becomes stronger as we move from the TOA to the SRF. Regarding the stratospheric layers, R^2 between RF_{NET} and AOD was found to be equal to 0.65 for the layers at the TOA, 0.76 for inside the AL, and 0.79 at SRF. Concerning the tropospheric layers, the corresponding R^2 values were found to be equal to 0.47, 0.57, and 0.84, revealing a very strong dependence near the ground. The layer observation height (CoM) seems not to be directly correlated with RF_{NET} (Figure 7III). However, the tropospheric layers presented a wide range of RF_{NET} values in all of the vertical levels, in contrast to the corresponding stratospheric layers' values, which showed less diversity.

Heinold et al. (2021) [67] found values up to +0.50 W/m^2 at the TOA and −0.81 W/m^2 at SRF direct radiative forcing averaged for the Southern Hemisphere during January 2020. Hirsch and Koren (2021) [22] derived a value of +1.10 W/m^2 in the latitude belt between 20° S and 60° S. Yu et al. (2021) [26] obtained an estimate for global annual average effective RF of −0.03 W/m^2 at TOA and −0.32 W/m^2 at the surface due to the smoke event. According to Chang et al. (2021) [67], the wildfire event was associated with a strongly negative RF between −14.80 and −17.7 W/m^2, which decreased the surface air temperature by about 3.7–4.4 °C.

Khaykin et al. (2020) [5] showed that, in the latitude band between 25° and 60° S, during February 2020, the RF was as large as about −1.00 W/m^2 at the TOA and −3.00 W/m^2 at the surface. From the perspective of the stratospheric aerosol-layer perturbation, the global TOA RF produced by the Australian fires (2019–2020) was greater than the RF produced by all documented wildfire events and of the same order of magnitude of moderate volcanic eruptions during the last three decades (that have an integrated effect estimated at −0.19 ± 0.09 W/m^2, or smaller).

We note here that the majority of the studies mentioned above present the RF as a mean value over a wide area and time period, in contrast to our study that focused on the forcing of each BB aerosol layer. Additionally, the average on the RF could have also affected the accuracy of the estimations, since the SZA information is lost, compared to this study in which the inclusion of the SZA provides a more precise approach.

Figure 7. Net radiative forcing values per case (illustrated by colored solid circles) at top of atmosphere (TOA) (**a**), inside the smoke layers (**b**), and at surface (SRF) (**c**), versus the SZA (**I**), the AOD (**II**), and the CoM (**III**) of the aerosol layers. The different colors correspond to the tropospheric (cyan) and stratospheric (magenta) BB aerosol layers, while the solid lines and shadowed areas correspond to the mean values and std of the RF_{NET} at TOA inside the layer and at the SRF.

4. Conclusions

The 2019–2020 extraordinary Australian bushfires injected large amounts of smoke particles into both the troposphere and stratosphere. This long-lasting BB event was studied within the time period ranging from 25 December 2019 to 12 February 2020, using range-resolved aerosol measurements performed by the CALIOP space-borne lidar instrument onboard the CALIPSO satellite. The smoke layers were analyzed in terms of their geometrical, optical, and radiative properties in different altitudes and regions, within the longitude range of 140° E to 20° W, in the latitude band of 20°–60° S, as they were transported from the Australian banks to the South American continent. In this transportation, the Andes mountain range possibly played an important role, acting similar to a physical barrier to the Pacific Ocean, forcing the aerosols to circulate, which resulted in them staying for longer time periods in the same longitude range.

The altitude of the smoke layers ranged from near ground and to the stratosphere, almost at the altitude of 22 km amsl. According to their main optical properties, the presented PLDR values replicated the same pattern over the regions, namely, lower values in the

troposphere and higher in the stratosphere. More specifically, concerning the tropospheric altitude categories, the mean value of PLDR were lower than 0.06, while the maximum value did not exceed 0.15, indicating the presence of nearly spherical particles in the smoke layers, possibly affected by increased RH as they were transported over the ocean. In the stratosphere, PLDR values as high as 0.20 were observed, and values indicative of irregular solid shapes were possibly driven by the acquired ice coating obtained in the stratosphere. As the smoke moved westerly, a slight decrease in tropospheric PLDR values was observed, in contrary to the enhanced PLDR values of the stratospheric aerosols.

Fine and ultrafine smoke particles ($Å_b$ values up to 3) were dominant in the stratosphere, while, in the troposphere, $Å_b$ values were found to be even below 1, indicating coarser particles. As the aerosol plume moved towards North America, a slightly descending trend was observed in the tropospheric $Å_b$ values, while the stratospheric $Å_b$ values were lightly increased, showing that these particles probably grew in size in the troposphere and shrank in the stratosphere, respectively, as they fended off the source.

Concerning the smoke AOD values, higher BB aerosol loads were recorded in the lower troposphere, compared to the upper atmosphere. A maximum AOD value of 0.54 was found in the lower troposphere over the fire spots, while AOD values reached up to 0.29 in the stratosphere. In general, stratospheric layers showed less diversity in their properties compared to the tropospheric ones. During the same time period, the CO concertation increased up to 100%, compared to the same days of the event averaged over a base period (2004–2019), mostly in the 700–950 hPa pressure levels. The highest observed increase in CO was 92% at 950 hPa over the first study region. Likewise, the O_3 enhancement presented values of 60–96% in the higher atmospheric pressure levels and even 100% in the lower ones (200–400 hPa). R^2 values between the relative change in the concentrations of CO and O_3 showed that the impact of emitted CO on the O_3 formation was mostly significant close to the fire source (GR), while, for the rest of the regions, CO variation did not play a key role in the observed O_3 enhancement.

In regard to the RF_{NET}, it presented a good correlation with the AOD values, which tends to become stronger from the TOA to SRF. Both the tropospheric (-12.83 to -32.22 W/m^2) and stratospheric (-7.36 to -18.51 W/m^2) RF_{NET} of the smoke layers were negative in each vertical atmospheric level (TOA, inside the aerosol layer, SRF), despite the fact that the tropospheric layers showed a higher impact than the stratospheric ones, especially on the SRF.

Finally, it is crucial to point out that the range-resolved aerosol measurements, provided by our study, presented a new perspective on this unique smoke event in three different aspects (spatially, temporally, and vertically), as the aerosol properties were studied in a wide area of the South Hemisphere, during a long-lasting time period, from ground level to the stratosphere.

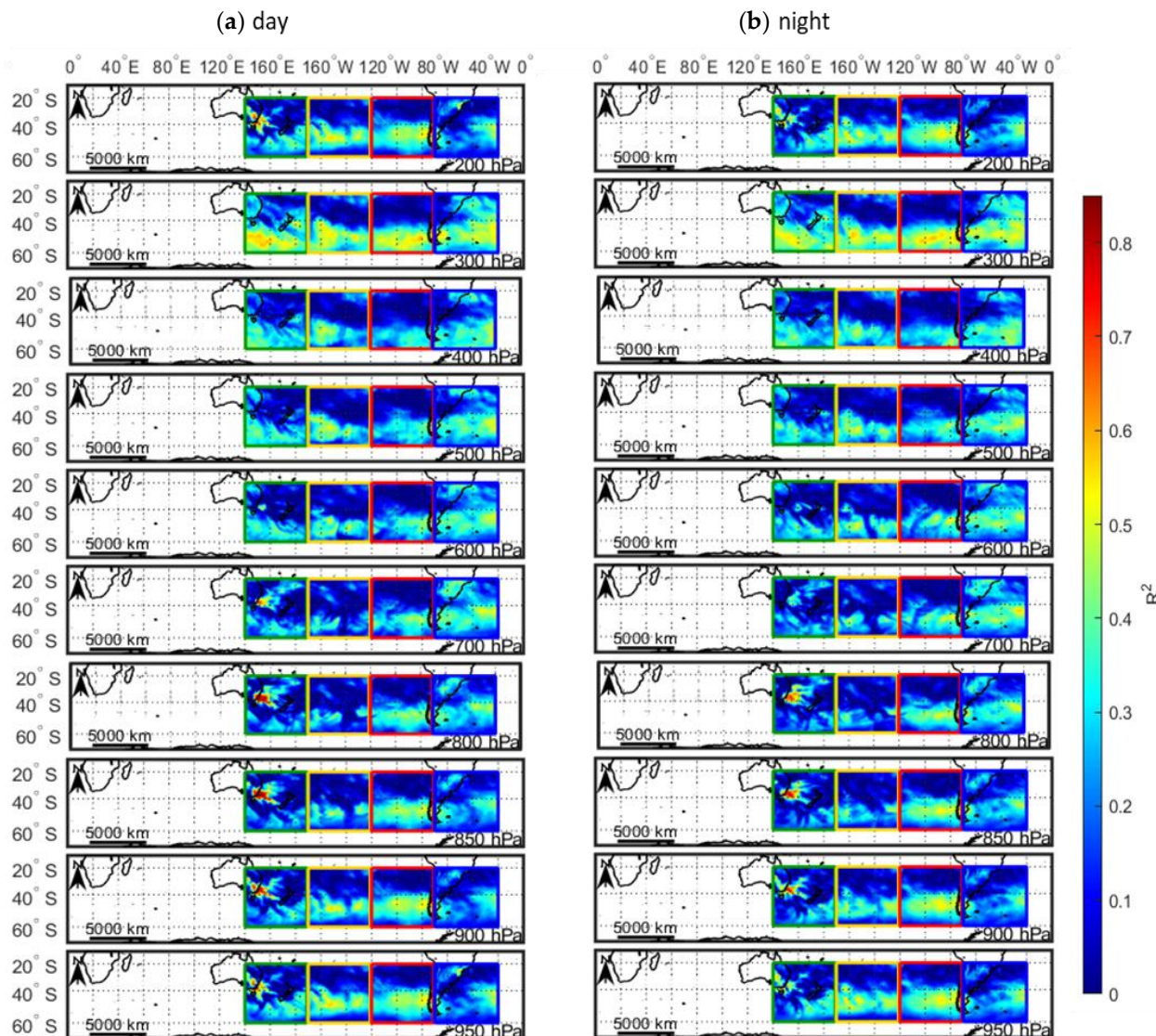**Conflicts of Interest:** The authors declare no conflict of interest.

Appendix A

Figure A1. Active fires in South America, as obtained by MODIS for the time period of December 2019–February 2020; the confidence of the fire spots was set to be above 70%.

Table A1. Mean values and std of the relative change of CO and O_3 as they were calculated per region and pressure level of the study area.

Pressure Level (hPa)	950	900	850	800	700	600	500	400	300	200
CO (%)										
GR	8 ± 14	8 ± 13	7 ± 14	6 ± 14	6 ± 14	9 ± 11	11 ± 10	12 ± 12	12 ± 14	14 ± 24
YR	14 ± 12	14 ± 13	14 ± 16	14 ± 18	15 ± 20	18 ± 22	18 ± 20	13 ± 14	8 ± 18	4 ± 21
RR	10 ± 9	10 ± 10	10 ± 11	12 ± 12	11 ± 10	13 ± 14	15 ± 15	17 ± 15	18 ± 19	12 ± 24
BR	3 ± 19	5 ± 22	7 ± 24	9 ± 24	13 ± 24	11 ± 20	8 ± 16	7 ± 16	7 ± 20	10 ± 27
O_3 (%)										
GR	3 ± 20	5 ± 19	9 ± 22	9 ± 21	8 ± 19	9 ± 17	7 ± 20	26 ± 28	2 ± 29	2 ± 36
YR	10 ± 17	8 ± 16	5 ± 17	7 ± 20	15 ± 21	14 ± 21	12 ± 21	32 ± 30	10 ± 38	18 ± 51
RR	9 ± 23	9 ± 19	8 ± 19	10 ± 20	11 ± 16	10 ± 16	7 ± 19	19 ± 31	2 ± 34	13 ± 44
BR	5 ± 21	6 ± 19	5 ± 17	6 ± 17	7 ± 17	8 ± 18	11 ± 20	26 ± 24	9 ± 35	12 ± 44

Figure A2. R^2 between CO and O_3 relative differences with respect to the base dataset at various pressure levels (950–200 hPa) (**a**) during day and (**b**) night.

References

1. Yang, X.; Zhao, C.; Yang, Y.; Yan, X.; Fan, H. Statistical Aerosol Properties Associated with Fire Events from 2002 to 2019 and a Case Analysis in 2019 over Australia. *Atmos. Chem. Phys.* **2021**, *21*, 3833–3853. [CrossRef]
2. Baars, H.; Ansmann, A.; Ohneiser, K.; Haarig, M.; Engelmann, R.; Althausen, D.; Hanssen, I.; Gausa, M.; Pietruczuk, A.; Szkop, A.; et al. The Unprecedented 2017–2018 Stratospheric Smoke Event: Decay Phase and Aerosol Properties Observed with EARLINET. *Atmos. Chem. Phys.* **2019**, *19*, 15183–15198. [CrossRef]
3. Ohneiser, K.; Ansmann, A.; Kaifler, B.; Chudnovsky, A.; Barja, B.; Knopf, D.A.; Kaifler, N.; Baars, H.; Seifert, P.; Villanueva, D.; et al. Australian Wildfire Smoke in the Stratosphere: The Decay Phase in 2020/21 and Impact on Ozone Depletion. *Atmos. Chem. Phys. Discuss.* **2022**, 1–41.
4. Ohneiser, K.; Ansmann, A.; Baars, H.; Seifert, P.; Barja, B.; Jimenez, C.; Radenz, M.; Teisseire, A.; Floutsi, A.; Haarig, M.; et al. Smoke of Extreme Australian Bushfires Observed in the Stratosphere over Punta Arenas, Chile, in January 2020: Optical Thickness, Lidar Ratios, and Depolarization Ratios at 355 and 532 Nm. *Atmos. Chem. Phys.* **2020**, *20*, 8003–8015. [CrossRef]
5. Khaykin, S.; Legras, B.; Bucci, S.; Sellitto, P.; Isaksen, L.; Tencé, F.; Bekki, S.; Bourassa, A.; Rieger, L.; Zawada, D.; et al. The 2019/20 Australian Wildfires Generated a Persistent Smoke-Charged Vortex Rising up to 35 Km Altitude. *Commun. Earth Environ.* **2020**, *1*, 22. [CrossRef]
6. Yang, X.; Zhao, C.; Yang, Y.; Fan, H. Long-Term Multi-Source Data Analysis about the Characteristics of Aerosol Optical Properties and Types over Australia. *Atmos. Chem. Phys.* **2021**, *21*, 3803–3825. [CrossRef]
7. Ansmann, A.; Ohneiser, K.; Mamouri, R.E.; Knopf, D.A.; Veselovskii, I.; Baars, H.; Engelmann, R.; Foth, A.; Jimenez, C.; Seifert, P.; et al. Tropospheric and Stratospheric Wildfire Smoke Profiling with Lidar: Mass, Surface Area, CCN, and INP Retrieval. *Atmos. Chem. Phys.* **2021**, *21*, 9779–9807. [CrossRef]
8. Zielinski, T.; Bolzacchini, E.; Cataldi, M.; Ferrero, L.; Graßl, S.; Hansen, G.; Mateos, D.; Mazzola, M.; Neuber, R.; Pakszys, P.; et al. Study of Chemical and Optical Properties of Biomass Burning Aerosols during Long-Range Transport Events toward the Arctic in Summer 2017. *Atmosphere* **2020**, *11*, 84. [CrossRef]
9. Ponczek, M.; Franco, M.A.; Carbone, S.; Rizzo, L.V.; Monteiro, D.; Morais, F.G.; Duarte, A.; Barbosa, H.M.J.; Artaxo, P. Environmental Science: Linking the Chemical Composition and Optical Properties of Biomass Burning Aerosols in Amazonia. *Environ. Sci. Atmos.* **2022**, *2*, 252–269. [CrossRef]
10. Müller, D.; Mattis, I.; Ansmann, A.; Wandinger, U.; Ritter, C.; Kaiser, D. Multiwavelength Raman Lidar Observations of Particle Growth during Long-Range Transport of Forest-Fire Smoke in the Free Troposphere. *Geophys. Res. Lett.* **2007**, *34*. [CrossRef]
11. Haarig, M.; Ansmann, A.; Baars, H.; Jimenez, C.; Veselovskii, I.; Engelmann, R.; Althausen, D. Depolarization and Lidar Ratios at 355, 532, and 1064 Nm and Microphysical Properties of Aged Tropospheric and Stratospheric Canadian Wildfire Smoke. *Atmos. Chem. Phys.* **2018**, *18*, 11847–11861. [CrossRef]
12. Hu, Q.; Goloub, P.; Veselovskii, I.; Bravo-Aranda, J.A.; Elisabeta Popovici, I.; Podvin, T.; Haeffelin, M.; Lopatin, A.; Dubovik, O.; Pietras, C.; et al. Long-Range-Transported Canadian Smoke Plumes in the Lower Stratosphere over Northern France. *Atmos. Chem. Phys.* **2019**, *19*, 1173–1193. [CrossRef]
13. Levine, J.S. Biomass Burning: The Cycling of Gases and Particulates from the Biosphere to the Atmosphere. *Treatise Geochem. Second Ed.* **2013**, *5*, 139–150. [CrossRef]
14. Akagi, S.K.; Yokelson, R.J.; Burling, I.R.; Meinardi, S.; Simpson, I.; Blake, D.R.; McMeeking, G.R.; Sullivan, A.; Lee, T.; Kreidenweis, S.; et al. Measurements of Reactive Trace Gases and Variable O3 Formation Rates in Some South Carolina Biomass Burning Plumes. *Atmos. Chem. Phys.* **2013**, *13*, 1141–1165. [CrossRef]
15. Liu, J.C.; Mickley, L.J.; Sulprizio, M.P.; Dominici, F.; Yue, X.; Ebisu, K.; Anderson, G.B.; Khan, R.F.A.; Bravo, M.A.; Bell, M.L. Particulate Air Pollution from Wildfires in the Western US under Climate Change. *Clim. Chang.* **2016**, *138*, 655–666. [CrossRef]
16. Brey, S.J.; Fischer, E.V. Smoke in the City: How Often and Where Does Smoke Impact Summertime Ozone in the United States? *Environ. Sci. Technol.* **2016**, *50*, 1288–1294. [CrossRef]
17. Jaffe, D.A.; Wigder, N.; Downey, N.; Pfister, G.; Boynard, A.; Reid, S.B. Impact of Wildfires on Ozone Exceptional Events in the Western U.S. *Environ. Sci. Technol.* **2013**, *47*, 11065–11072. [CrossRef]
18. Jaffe, D.A.; Cooper, O.R.; Fiore, A.M.; Henderson, B.H.; Tonnesen, G.S.; Russell, A.G.; Henze, D.K.; Langford, A.O.; Lin, M.; Moore, T. Scientific Assessment of Background Ozone over the U.S.: Implications for Air Quality Management. *Elementa* **2018**, *6*, 56. [CrossRef]
19. Bourgeois, I.; Peischl, J.; Andrew Neuman, J.; Brown, S.S.; Thompson, C.R.; Aikin, K.C.; Allen, H.M.; Angot, H.; Apel, E.C.; Baublitz, C.B.; et al. Large Contribution of Biomass Burning Emissions to Ozone throughout the Global Remote Troposphere. *Proc. Natl. Acad. Sci. USA* **2021**, *118*, e2109628118. [CrossRef]
20. Selimovic, V.; Yokelson, R.J.; McMeeking, G.R.; Coefield, S. Aerosol Mass and Optical Properties, Smoke Influence on O_3, and High NO_3 Production Rates in a Western U.S. City Impacted by Wildfires. *J. Geophys. Res. Atmos.* **2020**, *125*, e2020JD032791. [CrossRef]
21. Filkov, A.I.; Ngo, T.; Matthews, S.; Telfer, S.; Penman, T.D. Impact of Australia's Catastrophic 2019/20 Bushfire Season on Communities and Environment. Retrospective Analysis and Current Trends. *J. Saf. Sci. Resil.* **2020**, *1*, 44–56. [CrossRef]
22. Hirsch, E.; Koren, I. Record-Breaking Aerosol Levels Explained by Smoke Injection into the Stratosphere. *Science* **2021**, *371*, 1269–1274. [CrossRef] [PubMed]

23. Kablick, G.P.; Allen, D.R.; Fromm, M.D.; Nedoluha, G.E. Australian PyroCb Smoke Generates Synoptic-Scale Stratospheric Anticyclones. *Geophys. Res. Lett.* **2020**, *47*, e2020GL088101. [CrossRef]
24. Peterson, D.A.; Campbell, J.R.; Hyer, E.J.; Fromm, M.D.; Kablick, G.P.; Cossuth, J.H.; DeLand, M.T. Wildfire-Driven Thunderstorms Cause a Volcano-like Stratospheric Injection of Smoke. *NPJ Clim. Atmos. Sci.* **2018**, *1*, 30. [CrossRef]
25. Yu, P.; Davis, S.M.; Toon, O.B.; Portmann, R.W.; Bardeen, C.G.; Barnes, J.E.; Telg, H.; Maloney, C.; Rosenlof, K.H. Persistent Stratospheric Warming Due to 2019–2020 Australian Wildfire Smoke. *Geophys. Res. Lett.* **2021**, *48*, e2021GL092609. [CrossRef]
26. Li, M.; Shen, F.; Sun, X. 2019–2020 Australian Bushfire Air Particulate Pollution and Impact on the South Pacific Ocean. *Sci. Rep.* **2021**, *11*, 12288. [CrossRef]
27. Kloss, C.; Sellitto, P.; Von Hobe, M.; Berthet, G.; Smale, D.; Krysztofiak, G.; Xue, C.; Qiu, C.; Jégou, F.; Ouerghemmi, I.; et al. Australian Fires 2019–2020: Tropospheric and Stratospheric Pollution Throughout the Whole Fire Season. *Front. Environ. Sci.* **2021**, *9*, 10-3389. [CrossRef]
28. Nguyen, H.D.; Azzi, M.; White, S.; Salter, D.; Trieu, T.; Morgan, G.; Rahman, M.; Watt, S.; Riley, M.; Chang, L.T.C.; et al. The Summer 2019–2020 Wildfires in East Coast Australia and Their Impacts on Air Quality and Health in New South Wales, Australia. *Int. J. Environ. Res. Public Health* **2021**, *18*, 3538. [CrossRef]
29. Tencé, F.; Jumelet, J.; Bekki, S.; Khaykin, S.; Sarkissian, A.; Keckhut, P. Australian Black Summer Smoke Observed by Lidar at the French Antarctic Station Dumont d'Urville. *J. Geophys. Res. Atmos.* **2022**, *127*, e2021JD035349. [CrossRef]
30. Giglio, L.; Schroeder, W.; Justice, C.O. The Collection 6 MODIS Active Fire Detection Algorithm and Fire Products. *Remote Sens. Environ.* **2016**, *178*, 31–41. [CrossRef]
31. Giglio, L.; Boschetti, L.; Roy, D.P.; Humber, M.L.; Justice, C.O. The Collection 6 MODIS Burned Area Mapping Algorithm and Product. *Remote Sens. Environ.* **2018**, *217*, 72–85. [CrossRef] [PubMed]
32. Inness, A.; Ades, M.; Agustí-Panareda, A.; Barr, J.; Benedictow, A.; Blechschmidt, A.M.; Jose Dominguez, J.; Engelen, R.; Eskes, H.; Flemming, J.; et al. The CAMS Reanalysis of Atmospheric Composition. *Atmos. Chem. Phys.* **2019**, *19*, 3515–3556. [CrossRef]
33. Flemming, J.; Benedetti, A.; Inness, A.; Engelen, J.R.; Jones, L.; Huijnen, V.; Remy, S.; Parrington, M.; Suttie, M.; Bozzo, A.; et al. The CAMS Interim Reanalysis of Carbon Monoxide, Ozone and Aerosol for 2003–2015. *Atmos. Chem. Phys.* **2017**, *17*, 1945–1983. [CrossRef]
34. Stohl, A.; Forster, C.; Frank, A.; Seibert, P.; Wotawa, G. Technical Note: The Lagrangian Particle Dispersion Model FLEXPART Version 6.2. *Atmos. Chem. Phys.* **2005**, *5*, 2461–2474. [CrossRef]
35. Pisso, I.; Sollum, E.; Grythe, H.; Kristiansen, N.I.; Cassiani, M.; Eckhardt, S.; Arnold, D.; Morton, D.; Thompson, R.L.; Groot Zwaaftink, C.D.; et al. The Lagrangian Particle Dispersion Model FLEXPART Version 10.4. *Geosci. Model Dev.* **2019**, *12*, 4955–4997. [CrossRef]
36. Solomos, S.; Gialitaki, A.; Marinou, E.; Proestakis, E.; Amiridis, V.; Baars, H.; Komppula, M.; Ansmann, A. Modeling and Remote Sensing of an Indirect Pyro-Cb Formation and Biomass Transport from Portugal Wildfires towards Europe. *Atmos. Environ.* **2019**, *206*, 303–315. [CrossRef]
37. Winker, D.M.; Vaughan, M.A.; Omar, A.; Hu, Y.; Powell, K.A.; Liu, Z.; Hunt, W.H.; Young, S.A. Overview of the CALIPSO Mission and CALIOP Data Processing Algorithms. *J. Atmos. Ocean. Technol.* **2009**, *26*, 2310–2323. [CrossRef]
38. Kim, M.H.; Omar, A.H.; Tackett, J.L.; Vaughan, M.A.; Winker, D.M.; Trepte, C.R.; Hu, Y.; Liu, Z.; Poole, L.R.; Pitts, M.C.; et al. The CALIPSO Version 4 Automated Aerosol Classification and Lidar Ratio Selection Algorithm. *Atmos. Meas. Tech.* **2018**, *11*, 6107–6135. [CrossRef] [PubMed]
39. Omar, A.H.; Winker, D.M.; Kittaka, C.; Vaughan, M.A.; Liu, Z.; Hu, Y.; Trepte, C.R.; Rogers, R.R.; Ferrare, R.A.; Lee, K.P.; et al. The CALIPSO Automated Aerosol Classification and Lidar Ratio Selection Algorithm. *J. Atmos. Ocean. Technol.* **2009**, *26*, 1994–2014. [CrossRef]
40. Young, S.A.; Vaughan, M.A.; Garnier, A.; Tackett, J.L.; Lambeth, J.D.; Powell, K.A. Extinction and Optical Depth Retrievals for CALIPSO's Version 4 Data Release. *Atmos. Meas. Tech.* **2018**, *11*, 5701–5727. [CrossRef]
41. Wainker, D.M.; Tackett, J.L.; Getzewich, B.J.; Liu, Z.; Vaughan, M.A.; Rogers, R.R. The Global 3-D Distribution of Tropospheric Aerosols as Characterized by CALIOP. *Atmos. Chem. Phys.* **2013**, *13*, 3345–3361. [CrossRef]
42. Ansmann, A.; Ohneiser, K.; Chudnovsky, A.; Baars, H.; Engelmann, R. CALIPSO Aerosol-Typing Scheme Misclassified Stratospheric Fire Smoke: Case Study From the 2019 Siberian Wildfire Season. *Front. Environ. Sci.* **2021**, *9*, 537. [CrossRef]
43. Bourgeois, Q.; Ekman, A.M.L.; Krejci, R. Aerosol Transport over the Andes from the Amazon Basin to the Remote Pacific Ocean: A Multiyear CALIOP Assessment. *J. Geophys. Res.* **2015**, *120*, 8411–8425. [CrossRef]
44. Papanikolaou, C.A.; Giannakaki, E.; Papayannis, A.; Mylonaki, M.; Soupiona, O. Canadian Biomass Burning Aerosol Properties Modification during a Long-Ranged Event on August 2018. *Sensors* **2020**, *20*, 5442. [CrossRef] [PubMed]
45. Noel, V.; Chepfer, H.; Hoareau, C.; Reverdy, M.; Cesana, G. Effects of Solar Activity on Noise in CALIOP Profiles above the South Atlantic Anomaly. *Atmos. Meas. Tech.* **2014**, *7*, 1597–1603. [CrossRef]
46. Zeng, Z.; Wang, Z.; Zhang, B. An Adjustment Approach for Aerosol Optical Depth Inferred from Calipso. *Remote Sens.* **2021**, *13*, 3085. [CrossRef]
47. Huang, L.; Jiang, J.H.; Tackett, J.L.; Su, H.; Fu, R. Seasonal and Diurnal Variations of Aerosol Extinction Profile and Type Distribution from CALIPSO 5-Year Observations. *J. Geophys. Res. Atmos.* **2013**, *118*, 4572–4596. [CrossRef]
48. Eloranta, E.W.; Piironen, P. Depolarization measurements with the high spectral resolution lidar. In Proceedings of the 17th ILRC, Sendai, Japan, 25–29 July 1994; Volume 63, pp. 147–168. [CrossRef]

49. She, C.-Y. Spectral Structure of Laser Light Scattering Revisited: Bandwidths of Nonresonant Scattering Lidars. *Appl. Opt.* **2001**, *40*, 4875. [CrossRef]

50. Behrendt, A.; Nakamura, T. Calculation of the Calibration Constant of Polarization Lidar and Its Dependency on Atmospheric Temperature. *Opt. Express* **2002**, *10*, 805. [CrossRef]

51. Emde, C.; Buras-Schnell, R.; Kylling, A.; Mayer, B.; Gasteiger, J.; Hamann, U.; Kylling, J.; Richter, B.; Pause, C.; Dowling, T.; et al. The LibRadtran Software Package for Radiative Transfer Calculations (Version 2.0.1). *Geosci. Model Dev.* **2016**, *9*, 1647–1672. [CrossRef]

52. Anderson, G.; Clough, S.; Kneizys, F. *AFGL Atmospheric Constituent Profiles*; AFGL-TR-86-0110; Defense Technical Information Center: Fort Belvoir, VA, USA, 1986; 46p.

53. Soupiona, O.; Papayannis, A.; Kokkalis, P.; Foskinis, R.; Sánchez Hernández, G.; Ortiz-Amezcua, P.; Mylonaki, M.; Papanikolaou, C.A.; Papagiannopoulos, N.; Samaras, S.; et al. EARLINET Observations of Saharan Dust Intrusions over the Northern Mediterranean Region (2014–2017): Properties and Impact on Radiative Forcing. *Atmos. Chem. Phys.* **2020**, *20*, 15147–15166. [CrossRef]

54. Kokkalis, P.; Soupiona, O.; Papanikolaou, C.A.; Foskinis, R.; Mylonaki, M.; Solomos, S.; Vratolis, S.; Vasilatou, V.; Kralli, E.; Anagnou, D.; et al. Radiative Effect and Mixing Processes of a Long-Lasting Dust Event over Athens, Greece, during the COVID-19 Period. *Atmosphere* **2021**, *12*, 318. [CrossRef]

55. Mona, L.; Amodeo, A.; Pandolfi, M.; Pappalardo, G. Saharan Dust Intrusions in the Mediterranean Area: Three Years of Raman Lidar Measurements. *J. Geophys. Res. Atmos.* **2006**, *111*, 1–13. [CrossRef]

56. Campetella, C.M.; Vera, C.S. The Influence of the Andes Mountains on the South American Low-Level Flow. *Geophys. Res. Lett.* **2002**, *29*, 6–9. [CrossRef]

57. Garreaud, R.D.; Molina, A.; Farias, M. Andean Uplift, Ocean Cooling and Atacama Hyperaridity: A Climate Modeling Perspective. *Earth Planet. Sci. Lett.* **2010**, *292*, 39–50. [CrossRef]

58. Burton, S.P.; Ferrare, R.A.; Vaughan, M.A.; Omar, A.H.; Rogers, R.R.; Hostetler, C.A.; Hair, J.W. Aerosol Classification from Airborne HSRL and Comparisons with the CALIPSO Vertical Feature Mask. *Atmos. Meas. Tech.* **2013**, *6*, 1397–1412. [CrossRef]

59. Mylonaki, M.; Papayannis, A.; Papanikolaou, C.-A.; Foskinis, R.; Soupiona, O.; Maroufidis, G.; Anagnou, D.; Kralli, E. Tropospheric Vertical Profiling of the Aerosol Backscatter Coefficient and the Particle Linear Depolarization Ratio for Different Aerosol Mixtures during the PANACEA Campaign in July 2019 at Volos, Greece. *Atmos. Environ.* **2021**, *247*, 118184. [CrossRef]

60. Tan, I.; Storelvmo, T.; Choi, Y.S. Spaceborne Lidar Observations of the Ice-Nucleating Potential of Dust, Polluted Dust, and Smoke Aerosols in Mixed-Phase Clouds. *J. Geophys. Res.* **2014**, *119*, 6653–6665. [CrossRef]

61. Vaughan, G.; Draude, A.P.; Ricketts, H.M.A.; Schultz, D.M.; Adam, M.; Sugier, J.; Wareing, D.P. Transport of Canadian Forest Fire Smoke over the UK as Observed by Lidar. *Atmos. Chem. Phys.* **2018**, *18*, 11375–11388. [CrossRef]

62. Qin, Y.; Ye, J.; Ohno, P.; Zhai, J.; Han, Y.; Liu, P.; Wang, J.; Zaveri, R.A.; Martin, S.T. Humidity Dependence of the Condensational Growth of α-Pinene Secondary Organic Aerosol Particles. *Environ. Sci. Technol.* **2021**, *55*, 14360–14369. [CrossRef]

63. Zhang, L.; Sun, J.Y.; Shen, X.J.; Zhang, Y.M.; Che, H.; Ma, Q.L.; Zhang, Y.W.; Zhang, X.Y.; Ogren, J.A. Observations of Relative Humidity Effects on Aerosol Light Scattering in the Yangtze River Delta of China. *Atmos. Chem. Phys.* **2015**, *15*, 8439–8454. [CrossRef]

64. Baylon, P.; Jaffe, D.A.; Wigder, N.L.; Gao, H.; Hee, J. Ozone Enhancement in Western US Wildfire Plumes at the Mt. Bachelor Observatory: The Role of NOx. *Atmos. Environ.* **2015**, *109*, 297–304. [CrossRef]

65. Lu, X.; Zhang, L.; Shen, L. Meteorology and Climate Influences on Tropospheric Ozone: A Review of Natural Sources, Chemistry, and Transport Patterns. *Curr. Pollut. Rep.* **2019**, *5*, 238–260. [CrossRef]

66. Heinold, B.; Baars, H.; Barja, B.; Christensen, M.; Kubin, A.; Ohneiser, K.; Schepanski, K.; Schutgens, N.; Senf, F.; Schrödner, R.; et al. Important Role of Stratospheric Injection Height for the Distribution and Radiative Forcing of Smoke Aerosol from the 2019/2020 Australian Wildfires. *Atmos. Chem. Phys. Discuss.* **2021**, 1–20.

67. Chang, D.Y.; Yoon, J.; Lelieveld, J.; Park, S.K.; Yum, S.S.; Kim, J.; Jeong, S. Direct Radiative Forcing of Biomass Burning Aerosols from the Extensive Australian Wildfires in 2019–2020. *Environ. Res. Lett.* **2021**, *16*, 044041. [CrossRef]